ACS APPLIED MATERIALS & INTERFACES

Research Article

www.acsami.org

Ir-Surface Enriched Porous Ir–Co Oxide Hierarchical Architecture for High Performance Water Oxidation in Acidic Media

Wei Hu,[†,‡] Huawei Zhong,[†] Wei Liang,[†] and Shengli Chen*[,†]

[†]Hubei Key Laboratory of Electrochemical Power Sources, Department of Chemistry, Wuhan University, Wuhan 430072, China

[‡]Hubei Collaborative Innovation Center for Advanced Organic Chemical Materials, Ministry of Education Key Laboratory for the Synthesis and Applications of Organic Functional Molecules, Hubei University, Wuhan 430062, China

Supporting Information

ABSTRACT: The large-scale application of acidic water electrolysis as a viable energy storage technology has been hindered by the high demand of precious metal oxides at anode to catalyze the oxygen evolution reaction (OER). We report an Ir–Co binary oxide electrocatalyst for OER fabricated by a multistep process of selective leaching of Co from Co-rich composite oxides prepared through thermal decomposition. The stepwise leaching of the Co component from the composites leads to the formation of macro- and mesoscale voids walled by a cross-linked nanoporous network of rod- and wedge-like building units of Ir–Co binary oxide with a rutile phase structure and an Ir-enriched surface. In comparison, Ir–Co binary oxide with similar composition prepared by direct thermal decomposition method exhibits a loose nanoparticle aggregation morphology with a Co-enriched surface. The cross-linked porous Ir–Co binary oxide from selective leaching is about 3-fold more active for the OER than that from direct thermal decomposition. Compared with pure IrO_2 from thermal decomposition, the Co-leached binary oxide is ca. two times more active and is much more durable during continuous oxygen evolution under a constant potential of 1.6 V, thus showing a possibility of reducing the demand of the expensive and scarce Ir in OER electrocatalyst for acidic water splitting.

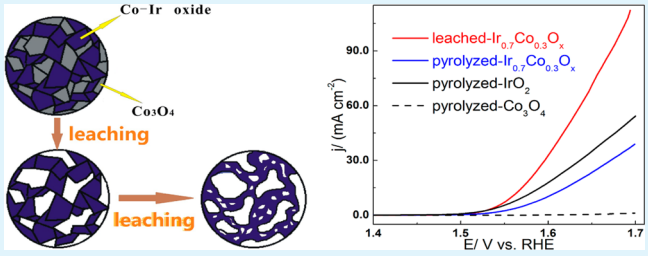

KEYWORDS: *oxygen evolution, water oxidation, acidic media, selective leaching, Ir-enriched*

1. INTRODUCTION

Electrolytic water splitting provides a carbon-free route to convert sporadic renewable electric powers into fuel.[1,2] The efficiency of this process is severely limited by the kinetics of the oxygen evolution reaction (OER). Therefore, great efforts have been made in finding an efficient electrocatalyst for the OER. Recently, a large body of oxide materials of earth-abundant transition metals has been explored;[3−11] the amorphous oxide layers deposited on conducting substrates through electrochemical[8,9] and photochemical[10,11] methods have shown considerable promise in cost-effective OER electrocatalysis. Most of these transition metal oxides can only be used in neutral and alkaline media because they are instable in acid media, while water electrolysis using proton exchange membrane (PEM) as electrolyte is more advantageous in several aspects such as energy efficiency, power density, and device compactness.[12]

Under the highly positive OER potentials in PEM analogue acidic media, most metals and metal oxides are instable or poorly conductive, except for rutile RuO_2 and IrO_2, which also have the best reported OER activity. In fact, even RuO_2 undergoes some dissolution during OER in acid.[13,14] Therefore, Ir oxide is the best choice for OER catalysts in acidic media, similar to that in PEM fuel cell in which Pt is required to catalyze the oxygen reduction reaction (ORR). Over the past two decades, we have seen a surge and great progress in developing Pt lean ORR electrocatalysts for PEM fuel cells;[15−18] however, material research in saving the even scarcer Ir in OER electrocatalysts for PEM water electrolysis considerably lags behind.

Recent reports have shown that the catalytic efficiency of Ir oxides for the OER can be significantly enhanced in the forms of ordered meso/macroporous structures,[19,20] electrochemically deposited nanoparticle films,[21−23] or amorphous films formed through photochemical deposition.[24] Alloying is also an effective route for saving the precious metals in catalysts. There have been considerable attempts in the last two decades to develop dimensionally stable anodes (DSAs) by alloying Ir oxides with acid-resistant non-noble metal oxides such as Ta_2O_5,[25] TiO_2,[26] SnO_2,[27] and so on. The resultant materials, however, generally showed inferior OER performance, unless Ir is richly contained (>80−70 mol %), mainly due to the OER inertia and poor conductivity of these non-noble metal oxides.

Oxide alloys with Ir-enriched surface are expected to achieve high OER activity and performance durability with reduced Ir content.[28,29] Selective leaching is an efficient approach to

Received: May 4, 2014
Accepted: July 1, 2014
Published: July 1, 2014

fabricate porous noble metals and their alloys[30−32] and has been applied in Pt-based ORR electrocatalysts.[33,34] In addition to the template-free pore formation, selective leaching is also capable of producing alloys with heterogeneously segregated composition (i.e., noble metal enriched surface). In this work, taking Ir−Co binary system for example, we demonstrate the application of selective leaching in fabricating Ir-surface enriched porous binary oxide and their superior OER electrocatalytic properties.

2. EXPERIMENTAL SECTION

2.1. Materials. $IrCl_3{\cdot}xH_2O$ (60 wt % Ir) was purchased from Shaanxi Kaida Chemical Engineering Co., Ltd., China. $CoCl_2{\cdot}6H_2O$, anhydrous ethanol, and hydrochloric acid were purchased from National Pharmaceutical Group Chemical Reagent Co., Ltd., China. All chemicals were analytical grade and used as received.

2.2. Materials Preparation. Oxide materials used in this study were prepared through either pyrolyzation or pyrolyzation followed by acid pickling. In a typical pyrolyzation preparation, required amounts of $IrCl_3{\cdot}xH_2O$ and $CoCl_2{\cdot}6H_2O$ were ultrasonically dissolved in 20 mL of anhydrous ethanol. The solution was heated at 60 °C and magnetically stirred until nearly complete evaporation of ethanol was achieved. The resulting precursor powder was then placed in a ceramic boat and heated at 450 °C for 1 h to allow complete pyrolysis of iridium or cobalt precursors. Finally, the prepared material was crushed to fine particles using an agate mortar. Pure oxides of IrO_2 and Co_3O_4 and Ir−Co composite oxides with Ir/Co molar ratios of 1:(1−4) and 0.7:0.3 have been prepared through this pyrolyzation method. Multiple acid pickling processes were applied to the Co-rich composite oxides with Ir/Co molar ratios of 1:(1−4) to allow leaching of Co. Briefly, the Co-rich composite oxide powders were dispersed in 5 mol L^{-1} HCl aqueous solution and stirred at 60 °C for 2 h. The dispersion was then allowed to sit for about 30 min until the supernatant became clear. After the supernatant was removed, the powders were dispersed in 5 mol L^{-1} HCl aqueous solution again for another Co-leaching process. The pickling process was repeated (typically 5 or 6 times) until no further Co dissolution could be seen. Black powders were then obtained through centrifugation and washed with deionized water, which was followed by drying at 100 °C in a vacuum oven for 12 h.

2.3. Physical Characterization. The morphologies of as-prepared materials were characterized with transmission electron microscopy (TEM, JEOL JEM-2010) working at an accelerating voltage of 200 kV and field emission scanning electron microscopy (FE-SEM, JEOL JSM-7100F). The physical surface areas and pore size distributions were determined through N_2 gas adsorption/desorption measurements (V-Sorb 2800P, Gold APP Instruments Corporation). The Brunauer−Emmett−Teller (BET) formulations were used to calculate the surface area. Pore size distribution was estimated by applying the Barrett−Joyner−Halenda (BJH) method to the desorption branch of the isotherm. The crystallinity and phase purity of the prepared samples were confirmed using an X'Pert Pro (PANalytical) X-ray diffractometer with Cu Kα radiation (λ = 1.5406 Å) operating at 40 kV and 40 mA. The chemical composition of as-prepared materials were analyzed using X-ray energy dispersive spectroscopy on a Hitachi S4800 scanning electron microscope (SEM) equipped with a Nanotrace EDX detector (Thermo Electron) and X-ray fluorescence (XRF) on a Shimadzu EDX-720 energy dispersive fluorescence spectrometer with Si semiconductor detector. The surface elemental composition and chemical state were analyzed by X-ray photoelectron spectroscopy (XPS, Kratos Ltd. XSAM800) with Mg−Kα radiation (1253.6 eV). Quantification of the surface elemental concentrations was accomplished by correcting photoelectron peak intensities for their cross sections, analyzer transmission function, and dependence of inelastic mean free paths of electrons on their kinetic energy.

2.4. Electrochemical Characterization. Electrochemical tests were carried out in a three-electrode system at room temperature with 0.5 mol L^{-1} H_2SO_4 as electrolyte solution, Pt foil as the counter electrode, and a saturated calomel electrode (SCE) as the reference electrode. However, the potentials in this paper are quoted with respect to reversible hydrogen electrode (RHE). The working electrode was a glassy carbon (GC, 5 mm diameter) rotating disk electrode (RDE) coated with the material to be tested. To prepare working electrodes, the tested material (5 mg) was dispersed in 1 mL of Nafion-contained isopropanol (1% in volume) to form catalyst ink. The required volume of ink was then pasted on the prepolished GC RDE electrode. Cyclic voltammograms (CVs) were recorded in a potential window between 0.4 and 1.4 V at a potential scanning rate of 50 mV s^{-1} in argon-saturated solution. Steady-state polarization curves for OER were recorded in O_2-saturated solution by rotating the working electrode at an electrode rotation rate of 1600 rpm and a using a potential scanning rate of 5 mV s^{-1}. Before each measurement, the electrode was electrochemically polished by performing 20 cycles of potential cycling between 0.0 and 1.4 V at a potential scanning rate of 500 mV s^{-1}. The CVs and steady-state polarization curves were recorded using a Bio-Logic potentiostat (VMP3) at room temperature (25 °C). The electrochemical impedance spectra (EIS) measurements were conducted on an Autolab potentiostat in the frequency range of 10 kHz to 0.01 Hz at the potential of 1.6 V (vs RHE) with an electrode rotation rate of 1600 rpm. A 10 mV amplitude of sinusoidal potential perturbation was employed in EIS measurements.

3. RESULTS AND DISCUSSION

3.1. Formation of Ir-Surface Enriched Porous Ir−Co Binary Oxide through Selective Leaching. Figure 1 schematically depicts the formation of Ir-surface enriched porous Ir−Co binary oxide through selective leaching of Co from Co-rich Ir−Co composite oxides. The fabrication process is started with pyrolyzation of a precursor mixture of $IrCl_3{\cdot}xH_2O$ and $CoCl_2{\cdot}6H_2O$ to form Co-rich Ir/Co composite oxides of two segregated phases: a Co oxide phase and an Ir−Co binary oxide phase. The biphase composite oxide is then subjected to multiple processes of acid pickling to selectively leach off the Co component. The phase-segregated Co oxides should dissolve immediately in the first two pickling processes, forming a macroporous Ir−Co binary oxide, from which further selective leaching of Co results in cross-linked meso/nanoporous Ir−Co binary oxide walls with Ir-enriched surface.

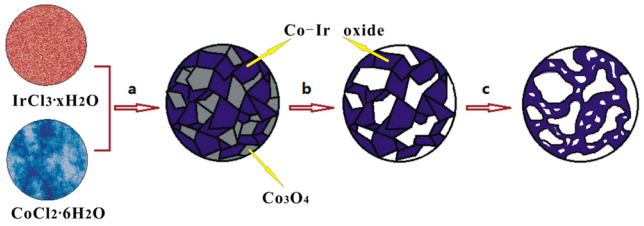

Figure 1. Schematic illustration of the formation process of (a) biphase Ir/Co composite oxide through pyrolyzation, (b) macro/mesoporous Ir−Co binary oxide due to dissolution of phase-segregated Co oxide, and (c) Ir-enriched surface and nanoporous walls through further Co dissolution and rearrangement of the remaining noble metal atoms.

The Ir/Co molar ratios in the prepared oxides were determined both through the selected-area EDX (SA-EDX) along with SEM characterization and through EDX in XRF equipment (XRF-EDX). For the oxides obtained by direct pyrolyzation, both of the two EDX measurements gave Ir/Co molar ratios that were very close to what we expected from the feeding amounts of the precursors (Table 1). Therefore, the EDX compositions were used to denote the prepared oxides, with the prefixes "pyrolyzed-" or "leached-" referring to samples

Table 1. Chemical Composition (Ir/Co Molar Ratio) Of the Prepared Oxides Determined by XRF, EDX, and XPS

oxide samples		nominal Ir/Co ratios	actual Ir/Co ratios		
			XRF-EDX	SA-EDX	XPS
pyrolyzed-$Ir_{0.7}Co_{0.3}O_x$		7:3	0.69:0.31	0.73:0.27	0.57:0.43
pyrolyzed-$IrCoO_x$	*a*	1:1	0.48:0.52	0.49:0.51	0.49:0.51
	b		0.67:0.33	0.70:0.30	0.87:0.13
pyrolyzed-$IrCo_2O_x$	*a*	1:2	0.31:0.69	0.38:0.62	0.43:0.57
	b		0.68:0.32	0.72:0.28	0.88:0.12
pyrolyzed-$IrCo_3O_x$	*a*	1:3	0.23:0.77	0.24:0.76	0.26:0.74
	b		0.68:0.32	0.71:0.29	0.89:0.11
pyrolyzed-$IrCo_4O_x$	*a*	1:4	0.18:0.82	0.21:0.79	0.22:0.78
	b		0.70:0.30	0.74:0.26	0.86:0.14

[a]Before leaching. [b]After leaching.

prepared from direct pyrolyzation or Co-selective leaching, respectively. For Co-rich composite oxides initially with Ir/Co molar ratios from 1:1 to 1:4, a multistep process of Co leaching resulted in Ir−Co binary oxides with very similar Ir/Co ratios of ca. 0.7:0.3. This should be because the leaching produced an Ir-rich surface, which prevented the remaining Co component from dissolving.

Angle-resolved XPS is a sensitive surface analysis technique that provides element composition of a few nanometers of the surface of samples.[35] The XPS results (Figures S1 and S2, Supporting Information) indicated that the Ir/Co atom ratios in the leached-$Ir_{0.7}Co_{0.3}O_x$ were nearly 0.9:0.1, which is much higher than the EDX values, suggesting the enrichment of Ir in the near surface region.[28,29] In comparison, the pyrolyzed-$Ir_{0.7}Co_{0.3}O_x$ exhibited an XPS Ir/Co atom ratio of ca. 0.6:0.4. The relatively near-surface enrichment of Co in pyrolyzed-$Ir_{0.7}Co_{0.3}O_x$ may be understood in terms of the lower surface energy of Co compared to that of Ir.[36]

The transformation from biphase composite oxide to a binary oxide of single-phase through multiple acid leaching was indicated by the XRD patterns of the prepared oxide samples (Figure 2). Both the Co_3O_4 and IrO_2 diffraction features were seen in the XRD patterns of the as-prepared Co-rich composite oxides (e.g., pyrolyzed-$IrCo_2O_x$). The XRD patterns of the leached-$Ir_{0.7}Co_{0.3}O_x$, however, were very similar to the pure pyrolyzed-IrO_2, except for the slight shift of peak positions to higher 2θ values, which should be a result of lattice contraction

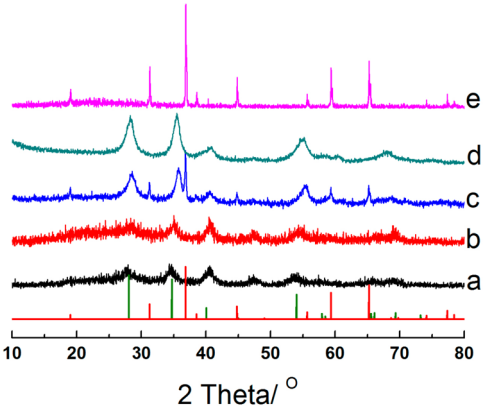

Figure 2. XRD patterns of the (a) pyrolyzed-IrO_2, (b) pyrolyzed-$Ir_{0.7}Co_{0.3}O_x$, (c) pyrolyzed-$IrCo_2O_x$, (d) leached-$Ir_{0.7}Co_{0.3}O_x$, and (e) pyrolyzed-Co_3O_4. The green and red lines give the characteristic peaks expected for the rutile IrO_2 (PDF #15-0870) and spinel Co_3O_4 (PDF #43-1003), respectively.

of IrO_2 due to Co doping. The leached-$Ir_{0.7}Co_{0.3}O_x$ and pyrolyzed-$Ir_{0.7}Co_{0.3}O_x$ exhibited similar XRD patterns due to the surface insensitive nature of XRD responses.

As shown by the SEM image in Figure 3a, the as-prepared Co-rich composite oxides were composed of large and dense

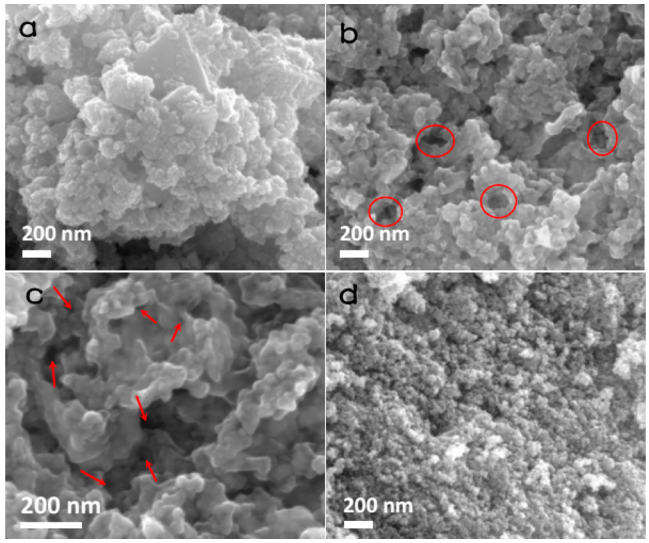

Figure 3. SEM images of (a) pyrolyzed-$IrCo_2O_x$ before leaching, (b and c) leached-$Ir_{0.7}Co_{0.3}O_x$, and (d) pyrolyzed-$Ir_{0.7}Co_{0.3}O_x$.

aggregates of crystalline particles of different shapes and relatively large sizes (from ~200 nm to several micrometers). After Co-selective leaching, the aggregates became obviously smaller and more discrete, forming a coral-like porous skeleton with pores of multiple scales (Figure 3b,c). In addition to the irregular macropores of different sizes (marked with circles in Figure 3b), there exist mesoscale pores inside and on the walls of the macropores (indicated by arrows in Figure 3c). In comparison, the pyrolyzed-$Ir_{0.7}Co_{0.3}O_x$ sample was composed of irregularly shaped aggregates of relatively smaller particles with no obvious porous network structure and relatively low degree of crystallinity (Figure 3d).

The porous structure of the leached-$Ir_{0.7}Co_{0.3}O_x$ was more clearly observed by the TEM images (Figure 4a−c), which showed voids of multiple scales (10−100 nm) and nanoporous walls of a few nanometers thickness constituted of aggregates of rod- and wedge-like basic building units. The nanoporous walls formed a cross-linked continuous network (Figure 4b), which should help to improve the electric conductivity due to the reduced grain boundary resistance. The nanorod building units

dx.doi.org/10.1021/am5027192 | ACS Appl. Mater. Interfaces 2014, 6, 12729−12736

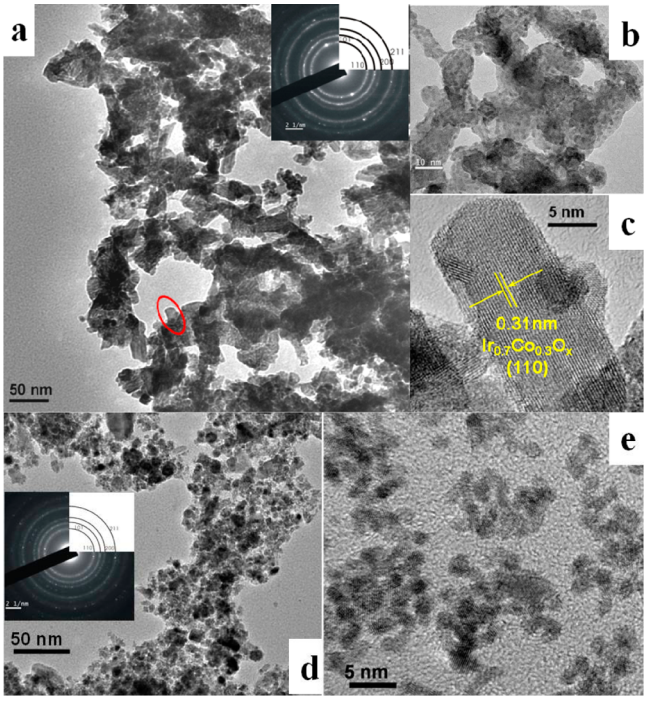

Figure 4. Typical TEM images of the (a–c) leached- and (d and e) pyrolyzed-$Ir_{0.7}Co_{0.3}O_x$. (a and d, insets) Selected area electron diffraction patterns of the corresponding samples.

showed lattice planes spaced ca. 0.31 nm apart (Figure 4c), which corresponds to the contracted (110) plane of IrO_2. As shown in Figure 4d–e, the pyrolyzed-$Ir_{0.7}Co_{0.3}O_x$ had morphology of loose aggregation of nanoparticles of 2–3 nm diameters. The TEM bright-field images with corresponding selected-area electron diffraction patterns for the two samples (Figure 4a,d insets) showed clear diffraction rings of rutile polycrystalline structure, with interplanar spacing distances slightly lower than the pyrolyzed-IrO_2 (Table S1, Supporting Information), which is in agreement with the XRD implication of Co-doping into the IrO_2 lattice.

N_2 adsorption/desorption isotherms and BJH pore-size distribution (Figure 5 and the inset) indicated that both pyrolyzed-$Ir_{0.7}Co_{0.3}O_x$ and leached-$Ir_{0.7}Co_{0.3}O_x$ show type IV hysteresis corresponding to the mesoporous characterization and the leached-$Ir_{0.7}Co_{0.3}O_x$ possessed pores of a range of

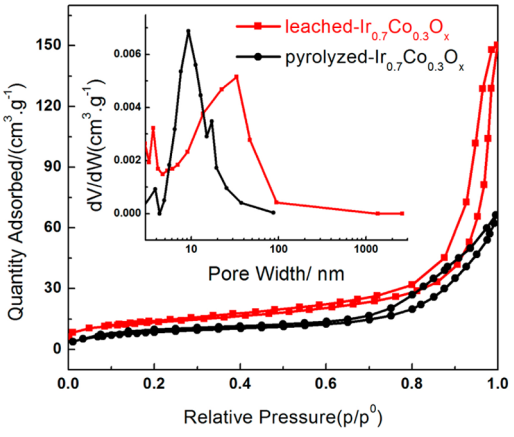

Figure 5. Isotherms and (inset) BJH pore-size distribution of the leached- and pyrolyzed-$Ir_{0.7}Co_{0.3}O_x$.

diameters from 10 to 100 nm, while the pyrolyzed-$Ir_{0.7}Co_{0.3}O_x$ contained small aggregate pores around 10 nm, agreeing well with the SEM and TEM observations. The BET surface area of the leached-$Ir_{0.7}Co_{0.3}O_x$ was ca. 47.2 $m^2\ g^{-1}$, which was ca. 1.5 times of that of the pyrolyzed-$Ir_{0.7}Co_{0.3}O_x$ (31.4 $m^2\ g^{-1}$).

3.2. Electrocatlytic Properties of the Ir-Surface Enriched Porous Ir–Co Binary Oxide. To assess the electrocatalytic properties of various oxide samples, they were deposited on a rotating-disk electrode (RDE) of GC. Such a thin-film RDE method has been widely used in assessing the electrocatalytic properties of powder materials.[37−39] A large number of studies have shown that as long as the catalyst film is not too thick (e.g., < 1 μm in thickness), the influence of porosity and thickness of the catalytic layer on the polarization curve is nearly negligible so that the voltammetric analysis developed for planar RDE can be used.[37−39] Therefore, we used a relatively low catalyst loading, namely, 0.102 mg cm^{-2}, which is close to those generally used in studying the oxygen reduction on Pt/C electrocatalysts. We first compared the cyclic voltammograms (CVs) of the leached-$Ir_{0.7}Co_{0.3}O_x$ and pyrolyzed-$Ir_{0.7}Co_{0.3}O_x$ in Ar-saturated acid solution (Figure 6).

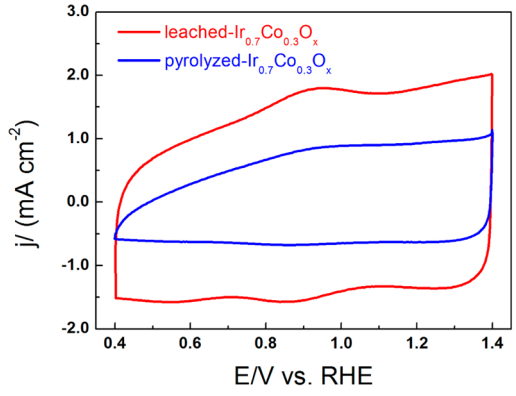

Figure 6. Representative cyclic voltammograms (CVs) in Ar-saturated 0.5 mol L^{-1} H_2SO_4 of the leached-$Ir_{0.7}Co_{0.3}O_x$ and pyrolyzed-$Ir_{0.7}Co_{0.3}O_x$. The currents are normalized by the geometric area of the GC substrate. Potential scanning rate: 50 mV s^{-1}. Catalyst loading: 102 μg cm^{-2}.

The redox and double layer charges on the CVs should represent the accessible electroactive surface areas (ESAs) of the corresponding samples. The CV charge exhibited by the leached-$Ir_{0.7}Co_{0.3}O_x$ (28.6 mC cm^{-2}) was more than 2 times higher than that given by the pyrolyzed-$Ir_{0.7}Co_{0.3}O_x$ (12.5 mC cm^{-2}), which was obviously higher than the difference in their BET surface areas. This should be a further evidence that the leached-$Ir_{0.7}Co_{0.3}O_x$ was more Ir-enriched on the surface.

As shown by the steady-state polarization curves in Figure 7a, the pyrolyzed-Co_3O_4 had negligible OER activity in acidic media, although it exhibited good electrocatalytic activity in alkaline media.[40,41] The pyrolyzed-$Ir_{0.7}Co_{0.3}O_x$ exhibited slightly lower OER current than the pyrolyzed-IrO_2 which also had a particle aggregate morphology (Figures S3 and S4, Supporting Information). The leached-$Ir_{0.7}Co_{0.3}O_x$, however, showed the highest activity among all samples, with a current density about 3 and 2 times higher than that of the pyrolyzed $Ir_{0.7}Co_{0.3}O_x$ and IrO_2, respectively, at potentials above 1.6 V. The overpotential at the current density of 0.5 mA cm^{-2} (with respect of the geometric area of GC substrate), which is a convention commonly used in OER literature to evaluate the

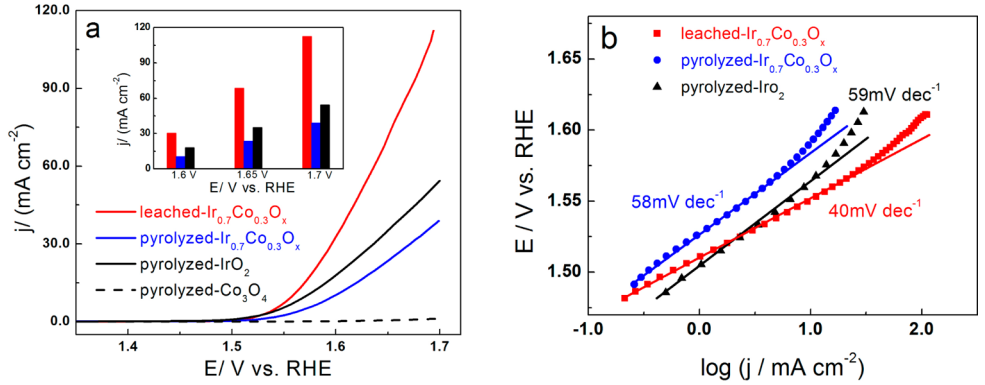

Figure 7. (a) Steady-state polarization curves obtained in O_2-saturated 0.5 mol L^{-1} H_2SO_4 (the inset shows the current densities at different potentials) and (b) the corresponding Tafel plots obtained by correcting the solution resistance (R_s) given by the electrochemical impedance spectra. The currents are normalized by the geometric area of the GC substrate. Electrode rotation rate: 1600 rpm. Catalyst loading: 102 μg cm^{-2}.

catalyst performance, was ca. 0.26 V for leached-$Ir_{0.7}Co_{0.3}O_x$, which is close to that recently reported for mesoporous IrO_2 film electrode (~0.25 V) prepared through electrodeposition,[21] but still considerably larger than that exhibited by the amorphous IrO_x film fabricated through photochemical deposition.[24] This should be because the present oxide materials have undergone a heat treatment at relatively high temperature (450 °C). It has been shown that thermal annealing can result in increased crystallinity, which would reduce the electrocatalytic activity of oxide materials toward the OER.[10,11,24] However, the increase in crystallinity may be beneficial to the long-term stability of the oxide electrocatalysts.

The OER current for the leached-$Ir_{0.7}Co_{0.3}O_x$ showed an obviously steeper increase with potential than did the pyrolyzed $Ir_{0.7}Co_{0.3}O_x$ and IrO_2. This was more clearly manifested by the Tafel plots shown in Figure 7b. The leached-$Ir_{0.7}Co_{0.3}O_x$ exhibited a Tafel slope of ca. 40 mV/dec, while the pyrolyzed-$Ir_{0.7}Co_{0.3}O_x$ and pyrolyzed-IrO_2 gave Tafel slopes close to 60 mV/dec. The ca. 60 mV/dec Tafel slopes have been usually reported for OER on Ir-based electrodes prepared by thermal decomposition,[42,43] while several recently reported Ir-based oxides have exhibited OER Tafel slopes around 40 mV/dec, for example, $Ir_{0.6}Sn_{0.4}O_2$ prepared by polyol method,[27] IrO_2 films prepared by Adams method,[44] and the amorphous IrO_2 film prepared by photochemical deposition.[24] The decrease in Tafel slope might be a result of the increased electric conductivity of the electrode materials or an altered reaction mechanism.[45−47] We believe that the electric conductivity is the major reason in the present case. The leached-$Ir_{0.7}Co_{0.3}O_x$ was not only more porous, but it also possessed a continuous phase of a cross-linked network of pore walls with Ir-enriched surface, which should result in much enhanced electric conductivity over the loosely aggregated particles of pyrolyzed oxides. The increased electric conductance would lower the overall electron transfer resistance in the catalyst film. Such an improved kinetic behavior is particularly valuable for large-scale application because the increase in the operation current density will cause a slower increase in overpotential and therefore high energy conversion efficiency.

The improved kinetics on the leached-$Ir_{0.7}Co_{0.3}O_x$ over the pyrolyzed oxides was also revealed by their electrochemical impedance spectra (EIS) obtained under OER conditions. Figure 8 shows the measured EIS for electrodes loaded with different oxide electrocatalysts and the equivalent circuit (EC)

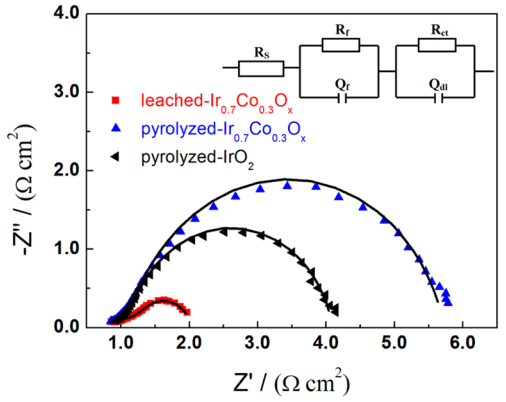

Figure 8. Experimental (scatters) and fitted (curves) EIS spectra for different oxide electrocatalysts at 1.6 V (vs RHE) with an electrode rotation rate of 1600 rpm. The inset shows the equivalent circuit used to fit the measured EIS.

used to fit the EIS. In the EC, R_s is the uncompensated solution resistance; the (R_f, Q_f) combination is associated with the physical processes of the oxide layer; and the components R_f and Q_f should, to some extent, represent the resistive and capacitive behaviors of the oxides, respectively. The (R_{ct}, Q_{dl}) combination is associated with the electrochemical processes at the oxide/solution interface, and the components R_{ct} and Q_{dl} refer to the reaction resistance and the electric double layer capacitance, respectively. This type of EC has been used quite often to simulate the impedance behaviors of metal oxide electrodes.[48−50] It can be seen that each EIS exhibits two strongly overlapped semicircles: one with smaller radii at high frequencies and one with large radii at relatively low frequencies. They should be associated with the (R_f, Q_f) and (R_{ct}, Q_{dl}) combinations, respectively. To get the best fit of the EIS, Q_f and Q_{dl} have to be treated as constant-phase-angle (CPA) elements rather than simple capacitive elements due to the complex capacitive behaviors of oxides.[48−50] For Q_{dl}, CPA factors very close to 1 can be used, whereas much smaller CPA factors (0.4−0.8) have to be used for Q_f. This indicated that Q_f values deviate pronouncedly from the behaviors of pure capacitance. A full understanding of the impedance behaviors of these oxides would be difficult and is beyond the scope of this study. We are mainly interested in R_{ct}, which represents the catalytic activity of the interested oxide for the OER.

dx.doi.org/10.1021/am5027192 | ACS Appl. Mater. Interfaces 2014, 6, 12729−12736

As seen in Figure 8, the radii of the low frequency semicircles (i.e., the R_{ct}) follow an order that leached-$Ir_{0.7}Co_{0.3}O_x$ < pyrolyzed-IrO_2 < pyrolyzed-$Ir_{0.7}Co_{0.3}O_x$, which agreed well with the OER activity order indicated by the voltammetric results shown above. The fitted R_{ct} values were 0.55, 2.71, and 4.24 Ω·cm^2, respectively. The R_{ct} differences between these materials were much higher than their ESA differences. For instance, the ESA of the leached-$Ir_{0.7}Co_{0.3}O_x$ was ca. 2 times higher than that of the pyrolyzed-$Ir_{0.7}Co_{0.3}O_x$, whereas the R_{ct} difference between the two oxides was more than 7 times. This suggested that the overall values of R_{ct} were not merely impacted by the catalytic activity of the oxide materials and that the electric conductivity may have significant contribution. The largely decreased R_{ct} value of the leached-$Ir_{0.7}Co_{0.3}O_x$ suggested that it had significantly enhanced electric conductivity over the pyrolyzed oxides. In addition, the fitted R_f values for the leached-$Ir_{0.7}Co_{0.3}O_x$, pyrolyzed-IrO_2, and pyrolyzed-$Ir_{0.7}Co_{0.3}O_x$, which were 0.27, 0.61, and 0.78, respectively, also indicated that the leached-$Ir_{0.7}Co_{0.3}O_x$ was more conductive in comparison with the pyrolyzed oxides.

In addition to higher electrocatalytic activity, the cross-linked and Ir surface enriched pore walls also resulted in superior stability of the leached oxide than the pyrolyzed ones, which is manifested by the chronoamperometric responses at a constant OER potential of 1.6 V (Figure 9). In addition to the rapid

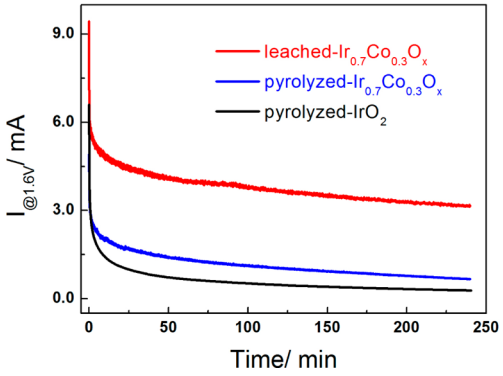

Figure 9. Chronoamperometric responses of the leached-$Ir_{0.7}Co_{0.3}O_x$, pyrolyzed-$Ir_{0.7}Co_{0.3}O_x$, and pyrolyzed-IrO_2 electrocatalysts under a constant polarization potential of 1.6 V in O_2-saturated 0.5 mol L^{-1} H_2SO_4. Electrode rotation rate: 1600 rpm. Catalyst loading: 127 μg cm^{-2}.

transient current decrease at the very beginning of potential step, the tested oxide electrocatalysts all exhibited a continuous OER activity decline in the course of the potentiostatic polarization. However, all along, the leached-$Ir_{0.7}Co_{0.3}O_x$ exhibited higher OER current than that of the pyrolyzed-$Ir_{0.7}Co_{0.3}O_x$ and IrO_2. Interestingly, even the pyrolyzed-$Ir_{0.7}Co_{0.3}O_x$ showed slightly higher OER current than the pure IrO_2, although it was initially less active. The degradation of the OER activity of Ir- and Ru-based oxides with time has been a commonly known phenomenon, which is believed to be due to the instability of high-valence Ir or Ru formed at the highly positive OER potentials.[13,51] The chronoamperometric responses shown in Figure 9 tend to suggest that the introduction of Co can increase the stability of Ir in the oxides, which is probably due to the anchoring effect of Co on Ir by forming alloy. One can find that the pyrolyzed-$Ir_{0.7}Co_{0.3}O_x$ exhibited relatively more rapid activity loss than did the pure IrO_2 in the later stage. This should be a result of the gradual dissolution of surface Co in pyrolyzed-$Ir_{0.7}Co_{0.3}O_x$, which was not Ir surface enriched as suggested by the XPS results. The dissolution of Co made the surface Ir lose anchoring agents. As for the leached-$Ir_{0.7}Co_{0.3}O_x$, on one hand, the Ir enriched surface structure rendered the Co components to be protected against dissolution in acid, and on the other hand, it made the surface Ir anchored by the underlying Co. Such a synergistic effect resulted in the superior stability of the leached-$Ir_{0.7}Co_{0.3}O_x$. In addition, as compared with the nanoparticle aggregates in the pyrolyzed-$Ir_{0.7}Co_{0.3}O_x$ and IrO_2, the porous structure with cross-linked pore walls in the leached-$Ir_{0.7}Co_{0.3}O_x$ should also benefit the stability.

4. CONCLUSIONS

A porous Ir−Co binary oxide electrocatalyst with Ir/Co molar ratio of about 0.7:0.3 has been synthesized through repeated Co-selective leaching of Co-rich composite oxide. The resulted binary oxide possesses a distinct structure of macro/mesoscale pores besieged by a cross-linked nanoporous wall network of rod- and wedge-like Ir−Co binary oxide with a rutile IrO_2 phase structure and Ir-enriched surface. It exhibits much lower charge transfer resistance and higher stability for the OER than does the Ir−Co binary oxide of similar composition and even the pure IrO_2 prepared through direct pyrolyzation, thus showing prospect in saving the precious metal Ir in the acidic water electrolysis.

■ ASSOCIATED CONTENT

Supporting Information

Details for the XPS analysis, SEM and TEM images for pyrolyzed-IrO_2, and interplanar spacing distances calculated from electron diffraction patterns. This material is available free of charge via the Internet at http://pubs.acs.org.

■ AUTHOR INFORMATION

Corresponding Author

*E-mail: slchen@whu.edu.cn. Tel: +86 027-68754693.

Notes

The authors declare no competing financial interest.

■ ACKNOWLEDGMENTS

This work is financially supported by the Ministry of Science and Technology of China (Grant Nos. 2012CB932800 and 2013AA110201), the National Natural Science Foundation of China (Grant No. 21073137), and the Hubei Key Laboratory of Fuel Cell (Wuhan University of Technology).

■ REFERENCES

(1) Edwards, P. P.; Kuznetsov, V. L.; David, W. I. F.; Brandon, N. P. Hydrogen and Fuel Cells: Towards a Sustainable Energy Future. *Energy Policy* **2008**, *36*, 4356−4362.

(2) deKrafft, K. E.; Wang, C.; Xie, Z.; Su, X.; Hinds, B. J.; Lin, W. Electrochemical Water Oxidation with Carbon-Grafted Iridium Complexes. *ACS Appl. Mater. Interfaces* **2012**, *4*, 608−613.

(3) Liu, X.; Chang, Z.; Luo, L.; Xu, T.; Lei, X.; Liu, J.; Sun, X. Hierarchical $Zn_xCo_{3-x}O_4$ Nanoarrays with High Activity for Electrocatalytic Oxygen Evolution. *Chem. Mater.* **2014**, *26*, 1889−1895.

(4) Jin, S.; Kevin, J. M.; Hubert, A. G.; John, B. G.; Yang, S. H. A Perovskite Oxide Optimized for Oxygen Evolution Catalysis from Molecular Orbital Principles. *Science* **2011**, *334*, 1383−1385.

(5) Tang, D.; Liu, J.; Wu, X.; Liu, R.; Han, X.; Han, Y.; Huang, H.; Liu, Y.; Kang, Z. Carbon Quantum Dot/NiFe Layered Double-

Hydroxide Composite as a Highly Efficient Electrocatalyst for Water Oxidation. *ACS Appl. Mater. Interfaces* **2014**, *6*, 7918−7925.
(6) Gao, M. R.; Xu, Y. F.; Jiang, J.; Zheng, Y. R.; Yu, S. H. Water Oxidation Electrocatalyzed by An Efficient $Mn_3O_4/CoSe_2$ Nanocomposite. *J. Am. Chem. Soc.* **2012**, *134*, 2930−2933.
(7) Singh, A.; Hocking, R. K.; Chang, S. L.-Y.; George, B. M.; Fehr, M.; Lips, K.; Schnegg, A.; Spiccia, L. Water Oxidation Catalysis by Nanoparticulate Manganese Oxide Thin Films: Probing the Effect of the Manganese Precursors. *Chem. Mater.* **2013**, *25*, 1098−1108.
(8) Kanan, M. W.; Nocera, D. G. In Situ Formation of an Oxygen-Evolving Catalyst in Neutral Water Containing Phosphate and Co^{2+}. *Science* **2008**, *321*, 1072−1075.
(9) Reece, S. Y.; Hamel, J. A.; Sung, K.; Jarvi, T. D.; Esswein, Arthur J.; Pijpers, J. J. H.; Nocera, D. G. Wireless Solar Water Splitting Using Silicon-Based Semiconductors and Earth-Abundant Catalysts. *Science* **2011**, *334*, 645−648.
(10) Smith, R. D. L.; Prevot, M. S.; Fagan, R. D.; Zhang, Z.; Sedach, P. A.; Siu, M. K. J.; Trudel, S.; Berlinguette, C. P. Photochemical Route for Accessing Amorphous Metal Oxide Materials for Water Oxidation Catalysis. *Science* **2013**, *340*, 60−63.
(11) Smith, R. D. L.; Prévot, M. S.; Fagan, R. D.; Trudel, S.; Berlinguette, C. P. Water Oxidation Catalysis: Electrocatalytic Response to Metal Stoichiometry in Amorphous Metal Oxide Films Containing Iron, Cobalt, and Nickel. *J. Am. Chem. Soc.* **2013**, *135*, 11580−11586.
(12) Parrondoa, J.; Argesa, C. G.; Niedzwieckib, M.; Andersonb, E. B.; Ayersb, K. E.; Ramani, V. Degradation of Anion Exchange Membranes Used for Hydrogen Production by Ultrapure Water Electrolysis. *RSC Adv.* **2014**, *4*, 9875−9879.
(13) Millet, P.; Dragoe, D.; Grigoriev, S.; Fateev, V.; Etievant, C. GenHyPEM: A Research Program on PEM Water Electrolysis Supported by the European Commission. *Int. J. Hydrogen Energy* **2009**, *34*, 4974−4982.
(14) Han, J. H.; Lee, S. W.; Kim, S. K.; Han, S.; Lee, W.; Hwang, C. S. Study on Initial Growth Behavior of RuO_2 Film Grown by Pulsed Chemical Vapor Deposition: Effects of Substrate and Reactant Feeding Time. *Chem. Mater.* **2012**, *24*, 1407−1414.
(15) Lee, E.; Jang, J. H.; Matin, M. A.; Kwon, Y. U. One-Step Sonochemical Syntheses of Ni@Pt Core-Shell Nanoparticles with Controlled Shape and Shell Thickness for Fuel Cell Electrocatalyst. *Ultrason. Sonochem.* **2014**, *21*, 317−323.
(16) Cheng, S.; Rettew, R. E.; Sauerbrey, M.; Alamgir, F. M. Architecture-Dependent Surface Chemistry for Pt Monolayers on Carbon-Supported Au. *ACS Appl. Mater. Interfaces* **2011**, *3*, 3948−3956.
(17) Dai, Y.; Ou, L.; Chen, S. Efficient and Superiorly Durable Pt-Lean Electrocatalysts of Pt−W Alloys for the Oxygen Reduction Reaction. *J. Phys. Chem. C* **2011**, *115*, 2162−2168.
(18) Stamenkovic, V. R.; Fowler, B.; Markovic, N. M. Improved Oxygen Reduction Activity on $Pt_3Ni(111)$ via Increased Surface Site Availability. *Science* **2007**, *315*, 493−497.
(19) Hu, W.; Wang, Y. Q.; Hu, X. H.; Zhou, Y. Q.; Chen, S. L. Three-Dimensional Ordered Macroporous IrO_2 as Electrocatalyst for Oxygen Evolution Reaction in Acidic Medium. *J. Mater. Chem.* **2012**, *22*, 6010−6016.
(20) Ortel, E.; Reier, T.; Strasser, P.; Kraehnert, R. Mesoporous IrO_2 Films Templated by PEO-PB-PEO Block-Copolymers: Self-Assembly, Crystallization Behavior, and Electrocatalytic Performance. *Chem. Mater.* **2011**, *23*, 3201−3209.
(21) Nakagawa, T.; Beasley, C. A.; Murray, R. W. Efficient Electro-Oxidation of Water near Its Reversible Potential by a Mesoporous IrO_x Nanoparticle Film. *J. Phys. Chem. C* **2009**, *113*, 12958−12961.
(22) Nakagawa, T.; Bjorge, N. S.; Murray, R. W. Electrogenerated IrO_x Nanoparticles as Dissolved Redox Catalysts for Water Oxidation. *J. Am. Chem. Soc.* **2009**, *131*, 15578−15579.
(23) Michaux, K. E.; Murray, R. W. Formation of Iridium(IV) Oxide (IrO_x) Films by Electroflocculation. *Langmuir* **2013**, *29*, 12254−12258.
(24) Smith, R. D. L.; Sporinova, B.; Fagan, R. D.; Trudel, S.; Berlinguette, C. P. Facile Photochemical Preparation of Amorphous Iridium Oxide Films for Water Oxidation Catalysis. *Chem. Mater.* **2014**, *26*, 1654−1659.
(25) Marshall, A.; Sunde, S.; Tsypkin, M.; Tunold, R. Performance of a PEM Water Electrolysis Cell Using Electrocatalysts for the Oxygen Evolution Electrode. *Int. J. Hydrogen Energy* **2007**, *32*, 2320−2324.
(26) Panic, V. V.; Dekanski, A. B.; Mitric, M. The Effect of the Addition of Colloidal Iridium Oxide into Sol-Gel Obtained Titanium and Ruthenium Oxide Coatings on Titanium on Their Electrochemical Properties. *Phys. Chem. Chem. Phys.* **2010**, *12*, 7521−7528.
(27) Marshall, A.; Børresen, B.; Hagen, G.; Tsypkin, M.; Tunold, R. Electrochemical Characterisation of $Ir_xSn_{1-x}O_2$ Powders as Oxygen Evolution Electrocatalysts. *Electrochim. Acta* **2006**, *51*, 3161−3167.
(28) Li, G.; Yu, H.; Wang, X.; Sun, S.; Li, Y.; Shao, Z.; Yi, B. Highly Effective $Ir_xSn_{1-x}O_2$ Electrocatalysts for Oxygen Evolution Reaction in the Solid Polymer Electrolyte Water Electrolyser. *Phys. Chem. Chem. Phys.* **2013**, *15*, 2858−2866.
(29) Li, G.; Yu, H.; Wang, X.; Yang, D.; Li, Y.; Shao, Z.; Yi, B. Triblock Polymer Mediated Synthesis of Ir−Sn Oxide Electrocatalysts for Oxygen Evolution Reaction. *J. Power Sources* **2014**, *249*, 175−184.
(30) Xu, C.; Wang, R.; Zhang, Y.; Ding, Y. A General Corrosion Route to Nanostructured Metal Oxides. *Nanoscale* **2010**, *2*, 906−909.
(31) Wang, R. Y.; Wang, C.; Cai, W. B.; Ding, Y. Ultralow-Platinum-Loading High-Performance Nanoporous Electrocatalysts with Nano-engineered Surface Structures. *Adv. Mater.* **2010**, *22*, 1845−1848.
(32) Déronzier, T.; Morfin, F.; Massin, L.; Lomello, M.; Rousset, J. L. Pure Nanoporous Gold Powder: Synthesis and Catalytic Properties. *Chem. Mater.* **2011**, *23*, 5287−5289.
(33) Wang, R.; Xu, C.; Bi, X.; Ding, Y. Nanoporous Surface Alloys as Highly Active and Durable Oxygen Reduction Reaction Electrocatalysts Energy. *Environ. Sci.* **2012**, *5*, 5281−5286.
(34) Oezaslan, M.; Heggen, M.; Strasser, P. Size-Dependent Morphology of Dealloyed Bimetallic Catalysts: Linking the Nano to the Macroscale. *J. Am. Chem. Soc.* **2012**, *134*, 514−524.
(35) Baer, D. R.; Engelhard, M. H. XPS Analysis of Nanostructured Materials and Biological Surface. *J. Electron Spectrosc. Relat. Phenom.* **2010**, *178−179*, 415−432.
(36) Skriver, H. L.; Rosengaard, N. M. Surface Energy and Work Function of Elemental Metals. *Phys. Rev. B: Condens. Matter Mater. Phys.* **1992**, *46*, 7157−7168.
(37) Schmidt, T. J.; Gasteiger, H. A. Rotating Thin-Film Method for Supported Catalysts; In *Handbook of Fuel Cells*; Vielstich, W., Gasteiger, H. A., Lamm, A., Eds.; Wiley: New York, 2003; p 316.
(38) Sun, Y.; Dai, Y.; Liu, Y.; Chen, S. A Rotating Disk Electrode Study of the Particle Size Effects of Pt for the Hydrogen Oxidation Reaction. *Phys. Chem. Chem. Phys.* **2012**, *14*, 2278−2285.
(39) Mayrhofer, K.; Strmcnik, D.; Blizanac, B. B.; Stamenkovic, V.; Arenz, M.; Markovic, N. M. Measurement of Oxygen Reduction Activities via the Rotating Disc Electrode Method: From Pt Model Surfaces to Carbon-Supported High Surface Area Catalysts. *Electrochim. Acta* **2008**, *53*, 3181−3188.
(40) Gerken, J. B.; McAlpin, J. G.; Chen, J. Y. C.; Rigsby, M. L.; Casey, W. H.; Britt, R. D.; Stahl, S. S. Electrochemical Water Oxidation with Cobalt-Based Electrocatalysts from pH 0−14: The Thermodynamic Basis for Catalyst Structure, Stability, and Activity. *J. Am. Chem. Soc.* **2011**, *133*, 14431−14442.
(41) Yeo, B. S.; Bell, A. T. Enhanced Activity of Gold-Supported Cobalt Oxide for the Electrochemical Evolution of Oxygen. *J. Am. Chem. Soc.* **2011**, *133*, 5587−5593.
(42) Da Silva, L. M.; Franco, D. V.; De Faria, L. A.; Boodts, J. F. C. Surface, Kinetics and Electrocatalytic Properties of $Ti/(IrO_2 + Ta_2O_5)$ Electrodes, Prepared Using Controlled Cooling Rate, for Ozone Production. *Electrochim. Acta* **2004**, *49*, 3977−3988.
(43) Reier, T.; Oezaslan, M.; Strasser, P. Electrocatalytic Oxygen Evolution Reaction (OER) on Ru, Ir, and Pt Catalysts: A Comparative Study of Nanoparticles and Bulk Materials. *ACS Catal.* **2012**, *2*, 1765−1772.

(44) Rasten, E.; Hagen, G.; Tunold, R. Electrocatalysis in Water Electrolysis with Solid Polymer Electrolyte. *Electrochim. Acta* **2003**, *48*, 3945−3952.
(45) Hu, J. M.; Zhang, J. Q.; Cao, C. N. Oxygen Evolution Reaction on IrO_2-based DSA® Type Electrodes: Kinetics Analysis of Tafel Lines and EIS. *Int. J. Hydrogen Energy* **2004**, *29*, 791−797.
(46) Siracusano, S.; Baglio, V.; Di Blasi, A.; Briguglio, N.; Stassi, A.; Ornelas, R.; Trifoni, E.; Antonucci, V.; Aricò, A. S. Electrochemical Characterization of Single Cell and Short Stack PEM Electrolyzers Based on a Nanosized IrO_2 Anode Electrocatalyst. *Int. J. Hydrogen Energy* **2010**, *35*, 5558−5568.
(47) De Faria, L. A.; Boodts, J. F. C.; Trasatti, S. Electrocatalytic Properties of Ternary Oxide Mixtures of Composition $Ru_{0.3}Ti_{0.7-x}Ce_xO_2$: Oxygen Evolution from Acidic Solution. *J. Appl. Electrochem.* **1996**, *26*, 1195−1199.
(48) Cheng, J. B.; Zhang, H. M.; Chen, G. B.; Zhang, Y. N. Study of $Ir_xRu_{1-x}O_2$ Oxides as Anodic Electrocatalysts for Solid Polymer Electrolyte Water Electrolysis. *Electrochim. Acta* **2009**, *54*, 6250−6256.
(49) Hou, Y. Y.; Hu, J. M.; Liu, L. J.; Zhang, Q.; Cao, C. N. Effect of Calcination Temperature on Electrocatalytic Activities of Ti/IrO_2 Electrodes in Methanol Aqueous Solutions. *Electrochim. Acta* **2006**, *51*, 6258−6267.
(50) Ye, F.; Li, J. L.; Wang, X. D.; Wang, T. T.; Li, S. M.; Wei, H. J.; Li, Q. F.; Christensen, E. Electrocatalytic Properties of $Ti/Pt-IrO_2$ Anode for Oxygen Evolution in PEM Water. *Electrolysis* **2010**, *35*, 8049−8055.
(51) Panić, V. V.; Nikolić, B. Ž. Electrocatalytic Properties and Stability of Titanium Anodes Activated by the Inorganic Sol−Gel Procedure. *J. Serb. Chem. Soc.* **2008**, *73*, 1083−1112.